A FOURIER–CHEBYSHEV SPECTRAL COLLOCATION METHOD FOR SIMULATING FLOW PAST SPHERES AND SPHEROIDS

RAJAT MITTAL*

Department of Mechanical Engineering, 237 MEB, University of Florida, Gainesville, FL 32611, USA

SUMMARY

An accurate Fourier–Chebyshev spectral collocation method has been developed for simulating flow past prolate spheroids. The incompressible Navier–Stokes equations are transformed to the prolate spheroidal co-ordinate system and discretized on an orthogonal body fitted mesh. The infinite flow domain is truncated to a finite extent and a Chebyshev discretization is used in the wall-normal direction. The azimuthal direction is periodic and a conventional Fourier expansion is used in this direction. The other wall-tangential direction requires special treatment and a restricted Fourier expansion that satisfies the parity conditions across the poles is used. Issues including spatial and temporal discretization, efficient inversion of the pressure Poisson equation, outflow boundary condition and stability restriction at the pole are discussed. The solver has been validated primarily by simulating steady and unsteady flow past a sphere at various Reynolds numbers and comparing key quantities with corresponding data from experiments and other numerical simulations. Copyright © 1999 John Wiley & Sons, Ltd.

1. INTRODUCTION

Unsteady separation and vortex shedding from three-dimensional bodies are intriguing phenomena that present us with a number of unanswered questions [1,2]. Such flows are encountered routinely in nature and in engineering applications, and therefore the importance of understanding these flows cannot be overemphasized. In particular, vortex shedding from particles assumes importance in particulate flows at high particle Reynolds numbers since this can have a significant effect on the enhancement of turbulence [3]. In most cases, particles can be modelled as spheres or spheroids, and therefore a detailed study of the vortex dynamics in spheroid wakes would improve our understanding of particle–turbulence interaction. These flows. however, do not lend themselves easily to experimental analysis or numerical simulations. Due to the inherent complexity of these flows, much of the data from experiments has been qualitative in nature. In fact, the bulk of our knowledge about three-dimensional separated wake flows rests on surface oil flow patterns [4] and dye visualization [5–8]. Advances in experimental techniques have, however, allowed researchers to obtain more quantitative information and recently detailed measurements of the wake of spheroids have been made [9,10].

---

* Correspondence to: Department of Mechanical Engineering, 237 MEB, University of Florida, Gainesville, FL 32611, USA.

Accurate numerical simulation of unsteady, separated flows past three-dimensional bodies is an expensive proposition and it is in fact difficult to find any well-documented, accurate simulations that solve the full equations of motion over spheroids without any approximations. In order to reduce the expense of these simulations, many researchers have limited themselves to solving the boundary/thin layer equations [11–16]. These simulations have added considerably to our knowledge of these flows. However, since the boundary layer approach cannot be extended to the separated region, few of these simulations have been able to provide detailed information in the separated wake region. Furthermore, most of the calculations have focussed on obtaining steady state solutions, and unsteady three-dimensional separation has for the most part not been addressed.

Spectral methods provide the highest accuracy on a per point basis and also allow for the possibility of using the intrinsic symmetries in the spheroidal geometry in developing an efficient solution procedure. The most natural approach to solving problems in spheroidal geometries is to use surface harmonic functions. For spherical geometries, the surface harmonic functions are the associated Legendre functions and these have been used in a variety of numerical studies in the past [17–19]. As demonstrated by Orszag [20], the main advantage of this approach is the absence of the 'pole problem'. However, since no fast transforms exist for surface harmonic functions this approach can be quite expensive. The spectral element method can also be used for simulating such flows and Tomboulides *et al.* [2] have used this method to simulate flow past a sphere up to a Reynolds number of 1000.

The possibility of using a double Fourier series on a sphere has been investigated by Orszag [20] and Fourier-based pseudo-spectral methods have been used for solving a number of relatively simple problems, like the shallow water equation [22], the two-dimensional Poisson equation [23] and surface flow [24]. The main advantages of this approach are simplicity, and the existence of the fast Fourier transform (FFT), which can result in a significant reduction in the computational expense. However, as pointed out by Orszag [20], the main disadvantage here is the existence of the 'pole problem' and the associated restriction on the time step for explicit time integration schemes.

Here a Fourier–Chebyshev spectral collocation based solver has been developed for direct numerical simulation of three-dimensional, viscous, incompressible flow past prolate spheroids. Flow past spheres can be solved as a special case. A number of issues including stability restriction at the pole, efficient inversion of the three-dimensional Poisson equation and non-reflective outflow boundary conditions have been addressed in developing the solver. A series of steady, as well as unsteady simulations of flow past a sphere have been performed using this solver and results compared with established experimental data. Three-dimensional flow visualizations of the sphere wake are used to demonstrate the fidelity with which the solver computes the complex vortex dynamics in these wake flows. Steady flow past a prolate spheroid has also been computed and comparisons made with available numerical results.

2. COMPUTATIONAL METHODOLOGY

The high accuracy of spectral methods make them attractive for flow simulations. However, it is usually quite difficult to apply these methods in complex geometries and most spectral simulations have consequently been limited to simple geometries [25]. Here we have developed a spectral collocation method for computing flow over spheroidal bodies. The method exploits special properties of the spheroidal co-ordinate system for constructing an algorithm that is efficient both in terms of CPU time and memory usage and should allow us to explore the

parameter space of the flow configuration. A description of the salient features of this algorithm is given in this section.

2.1. Spatial and temporal discretization

The basic shape that is considered is a prolate spheroid. The governing equations are the unsteady, incompressible Navier–Stokes equations given by

Continuity $\qquad \nabla \cdot \boldsymbol{u} = 0,$ (1)

Momentum conservation $\qquad \dfrac{\partial \boldsymbol{u}}{\partial t} + \boldsymbol{u} \cdot \nabla \boldsymbol{u} = -\nabla P + \dfrac{1}{Re_d} \nabla^2 \boldsymbol{u},$ (2)

where $\boldsymbol{u}$ and P are the velocity and pressure respectively. Furthermore, in the above equations, Re_d is the Reynolds number based on the freestream velocity (U_∞) and major axis of the spheroid, which is denoted by d. The above equations are transformed to the prolate spheroidal co-ordinate system where the mapping between the Cartesian (x, y, z) and prolate spheroidal (ξ, η, ϕ) co-ordinate systems (shown in Figure 1) is given by

$$x = a \cosh \xi \cos \eta, \qquad y = a \sinh \xi \sin \eta \cos \phi, \qquad z = a \sinh \xi \sin \eta \sin \phi, \tag{3}$$

where

$$\xi_{\text{body}} \le \xi \le \xi_{\text{outer}}, \qquad 0 \le \eta \le \pi, \qquad 0 \le \phi \le 2\pi, \tag{4}$$

and a is the distance between the centre and focii of the ellipsoid given by

$$a = \sqrt{1 - E^2}, \tag{5}$$

where E is the ratio of the minor to major axis of the ellipsoid. Thus, the parameter space of this flow consists of Reynolds number (Re_d), spheroid aspect ratio (E) and angle-of-attack (a).

The governing equations are discretized on an orthogonal curvilinear body-fitted grid for which the surface grid is shown in Figure 1. In the following discussion, N_ξ, N_η and N_ϕ are the number of grid points in the ξ-, η- and ϕ-directions respectively. The azimuthal direction ϕ is periodic over 2π and this allows us to use a Fourier collocation method in this direction. In the η-direction, which is referred to as the wall-tangential direction, the flow is periodic not over π but over 2π, and this allows us to use a Fourier collocation method for computing derivatives along this direction. It should be pointed out that care needs to be taken in calculating the η-derivatives of vector variables since vectors aligned along η and ϕ flip direction as one goes over the pole. The singularity in the co-ordinate transformation at the poles, which are located at $\eta = 0$ and π, can be avoided by distributing the collocation points
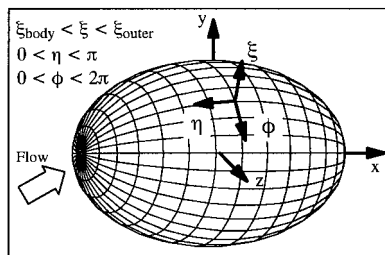

Figure 1. Surface mesh used in the current simulation. The Cartesian as well as the spheroidal co-ordinate systems are shown. The poles are located at $\eta = 0, \pi$.

in such a manner so as to avoid these locations. Thus, the collocation points in the wall-tangential direction are defined as

$$\eta_j = \frac{\pi}{N_\eta}\left(j - \frac{1}{2}\right); \quad j = 1, \ldots, N_\eta. \tag{6}$$

The semi-infinite flow domain is truncated to a large but finite distance and a Chebyshev collocation method is used in this non-periodic direction. The distribution of the Gauss–Lobatto collocation points is given by

$$\xi_i = \frac{1}{2}\cos\left[\frac{\pi(i-1)}{N_\xi - 1}\right](\xi_{\text{body}} - \xi_{\text{outer}}) + \frac{1}{2}(\xi_{\text{body}} + \xi_{\text{outer}}); \quad i = 1, 2, \ldots, N_\xi. \tag{7}$$

Thus, spectral discretization is used along all three directions and this results in a highly accurate computation of the derivatives.

A two-step time split [26–28] scheme is used for advancing the solution in time. The intermediate velocity field is obtained first by advancing through the advection–diffusion equation. A second-order-accurate, semi-implicit method is used for this step, where all convective terms are treated explicitly and diffusion terms are treated implicitly. Details regarding implicit treatment of diffusion terms will be provided in Section 2.3. A second-order Adams–Bashforth is employed for the explicit terms and the implicit terms are discretized using a Crank–Nicolson scheme. The next step is pressure-correction and this requires the solution of the pressure Poisson equation, which is solved with a homogeneous Neumann condition on the boundaries. Finally, the pressure-correction is added to the intermediate velocity and a divergence-free velocity field is obtained. A higher-order intermediate velocity boundary condition is used, which results in accurate imposition of the no-slip, no-penetration boundary condition on the body. Details of the time split scheme can be found in Mittal and Balachandar [28].

2.2. Outflow boundary conditions

Since the flow domain is truncated to a finite extent in the current simulations, appropriate boundary conditions are required at the outer boundary. Inviscid flow past the spheroid is computed first and this is used as the inflow boundary condition as well as the initial condition. The outflow boundary condition is not known *a priori* and a well-posed outflow boundary treatment has to be devised that will allow vortical disturbances to exit the domain with no significant reflection. A number of different non-reflective outflow boundary conditions have been used before with varying degree of success and the reader is referred to the paper of Sani and Gresho [29] for a comprehensive review on this topic. The global nature of the spectral methodology makes the simulation especially sensitive to boundary conditions and it has been found that simple boundary conditions that work well in conjunction with conventional finite difference methods can lead to catastrophic instability in spectral simulations [30]. A non-reflective boundary condition has been previously developed and tested in spectral simulations of flow past cylinders [28] and has been adapted for the current spheroid simulations. The approach is to smoothly parabolize the governing equations near the outflow boundary by multiplying the ξ-direction diffusion term with a smooth attenuation function. Thus, if the Laplacian operator can be written as a sum of one-dimensional operators along the three directions as $\nabla^2 \equiv \nabla^2_\xi + \nabla^2_\eta + \nabla^2_\phi$, then the diffusion term in the momentum equation (2) is modified as:

$$\frac{1}{Re_d}\nabla^2 u = \frac{1}{Re_d}[F(\xi,\eta)\nabla_\xi^2 + \nabla_\eta^2 + \nabla_\phi^2]\boldsymbol{u}. \tag{8}$$

Here, $F(\xi,\eta)$ is the attenuation function, which is equal to 1 in most of the domain and smoothly goes to 0 at the outflow boundary where the wake exits the computational domain. Thus, the governing equation is modified in a relatively small region near the outflow boundary and the impact of this on the flow in the upstream portion of the wake is minimal. The resultant parabolized equation does not require any outflow boundary condition and the governing equation can be solved at the outflow boundary. This boundary treatment has been tested extensively in previous work on cylindrical geometries and details of this test can be found in Mittal and Balachandar [28]. In the current simulations of flow past spheres it has been found that the boundary condition allows vortical disturbances to exit the computational domain in a smooth manner without any significant reflections.

2.3. Stability condition at the poles

Usually, the wall-normal spacing is extremely small near the body as compared with the grid spacing in wall-tangential directions and thus implicit treatment of just the wall-normal viscous term removes the viscous stability constraint to a large extent [28]. However, as can be seen from Figure 1, due to the topology of the grid, the azimuthal resolution increases tremendously at the poles, which are located at $\eta = 0$ and π. The azimuthal resolution near the poles is greater than the resolution at the equator by a factor of about $2N_\eta/\pi$. Therefore, for a typical mesh with $N_\eta = 80$, this implies that the ϕ resolution at the pole is higher than at the equator by a factor of about 50! Consequently, if the convection and diffusion terms in the ϕ-direction are treated explicitly it can lead to a severe stability constraint. However, implicit treatment of the non-linear convection terms and the cross-derivative terms is not desirable since it leads to coupled, non-linear operators that are computationally expensive to invert. Thus, other techniques have to be used in order to reduce the stability restriction.

Here we resort to low-pass filtering of the variables in the ϕ-direction near the poles, which allows us to reduce the 'effective' azimuthal resolution near the poles. At the end of the advection–diffusion time step, the intermediate velocity field is passed through a filter that removes the high wavenumber content. It should be pointed out that the filter cut-off varies in space with the most severe truncation occurring at the azimuthal gridline closest to the pole. Since the nominal azimuthal resolution near the poles is significantly higher than what is needed to resolve the flow gradients, it is expected that this filtering procedure will not have any significant effect on the accuracy of the computed flow. However, during the course of performing the various non-axisymmetric simulations of flow past a sphere presented here we have found that modes up to at least $k_\phi = 1$ need to be retained everywhere, since $k_\phi = 1$ is often the most unstable mode that leads to vortex shedding [34]. The filtering procedure mitigates the convective stability constraint to a large extent but the viscous stability constraint can still be quite severe near the poles and this necessitates implicit treatment of the viscous terms in the ϕ-direction. Implicit treatment of all components of the ϕ-direction viscous term leads to an operator that is quite expensive to invert. Instead, we identify that component of the ϕ-direction viscous term that is the largest near the poles (which is $1/\sin^2\eta$) and treat only this component implicitly. This leads to the following Helmholtz-like equation

$$\frac{F(\xi,\eta)}{\sinh\xi}\frac{\partial}{\partial\xi}\left(\sinh\xi\frac{\partial\boldsymbol{u}}{\partial\xi}\right) + \frac{1}{\sin^2\eta}\cdot\frac{\partial^2\boldsymbol{u}}{\partial\phi^2} - \frac{2Re}{\Delta t}\boldsymbol{u} = \boldsymbol{r}, \tag{9}$$

where $F(\xi, \eta)$ is the function that smoothly parabolizes the equation near the outflow boundary, and r contains all the explicit terms. Note that since the grid spacing in the η-direction is significantly larger near the body than in the other two directions, the viscous terms in this direction can be treated explicitly and this leads to a simpler operator on the left side of Equation (9). In fact, when the above equation is transformed in the ϕ-direction, we obtain a set of one-dimensional Helmholtz equations, which can be solved quite easily using the matrix diagonalization technique [31].

2.4. Inversion of the pressure Poisson equation

The pressure Poisson equation has to be solved in a fully implicit manner so as to exactly satisfy conservation of mass at the end of the full time step and fast inversion of the Poisson equation is the key to the overall viability of the solver. The ϕ-transformed pressure Poisson equation in prolate spheroidal co-ordinates can be written as:

$$\nabla^2 \hat{\Phi} = \frac{1}{h^2 \sinh \xi} \frac{\partial}{\partial \xi} \left(\sinh \xi \frac{\partial \hat{\Phi}}{\partial \xi} \right) + \frac{1}{h^2 \sin \eta} \frac{\partial}{\partial \eta} \left(\sinh \eta \frac{\partial \hat{\Phi}}{\partial \eta} \right) - \frac{k_\phi^2}{s^2} \hat{\Phi} = \hat{R}, \qquad (10)$$

where $\hat{R}$ denotes the right-hand-side of the equation, $\hat{\Phi}$ is the pressure that is solved for in the time split scheme, k_ϕ is the wavenumber in the ϕ-direction and

$$h^2 = a^2 (\sinh^2 \xi + \sin^2 \eta) \quad \text{and} \quad s^2 = a^2 \sinh^2 \xi \sin^2 \eta \qquad (11)$$

are the metrics of the transformation. Thus, in transformed space each azimuthal Fourier mode can be solved for separately. However, the curvilinear nature of the spheroidal co-ordinate system introduces non-constant coefficients into the Laplacian operator and transforming the equation in the η-direction results in a large set of coupled ODEs. Furthermore, unlike the elliptic co-ordinate system [28], the coupling here is of a broadband nature and the resultant matrix operator does not have a banded structure that can be exploited for devising a direct inversion technique. One approach is to use iterative methods like GMRES or multigrid, but then the efficiency of the inversion depends on a number of factors, including the choice of preconditioner and relaxation scheme. An efficient direct inversion procedure is clearly most desirable and here we have used the special properties of the metrics associated with the spheroidal system to devise a fast direct inversion procedure.

The key to the direct solution procedure lies in recognizing that the Laplacian operator in Equation (10) can be made separable by multiplying it by h^2. The matrix diagonalization procedure [31] can then be used to invert the operator directly. The attractiveness of this procedure lies in the fact that it requires a relatively small amount of storage and inversion can be accomplished through a series of matrix–vector multiplications. With the help of optimized linear algebra routines, this inversion can be accomplished quite efficiently.

It should also be pointed out that a conventional Fourier scheme cannot be used in the η-direction since variables are not periodic in that direction over the range $0-\pi$. Instead, we use a restricted Fourier series that employs a cosine series for the even ϕ modes and a sine series for the odd ϕ modes. When the pressure is expanded in terms of this restricted Fourier series, the 'parity' conditions at the pole [20,32] are satisfied exactly and a compact system of equations is obtained.

2.5. Grid clustering in the wake region

From the point of view of computational efficiency, it is desirable to provide enhanced resolution in the wake region, where flow gradients are large. In the current solver, a smooth
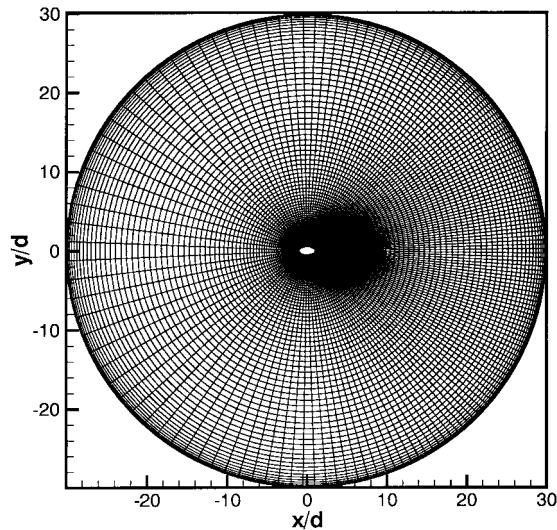
Figure 2. Typical grid used in the current simulation. Note that only a two-dimensional projection of the grid is shown. The three-dimensional grid can be obtained by rotating this mesh about the x-axis. For this mesh a value of γ equal to -0.35 is used to provide grid clustering in the wake, and this places 70% of the mesh points between $-\pi/2 < \eta < \pi/2$.

mapping is introduced in the η-direction that allows us to cluster more points in the wake region. The mapping used here is

$$\tan \tilde{\eta} = \frac{\sin \eta (1 - \gamma^2)}{\cos \eta (1 + \gamma^2) - 2\gamma}, \tag{12}$$

where $\tilde{\eta}$ represents the computational space with the clustered grid and γ is the parameter that controls the clustering. Values of γ used in the current simulation range between -0.4 and -0.2, with the larger negative value providing greater clustering in the wake. A typical mesh used in the current simulations is shown in Figure 2.

3. RESULTS AND DISCUSSION

Simulations of flow past a sphere at various Reynolds numbers have been used to test the spatial accuracy as well as to validate the solver. Simulations have been carried out in the axisymmetric as well as the non-axisymmetric regime and results compared with available experimental data. Numerical experimentation indicate that for simulation of flow past spheres, the solver is stable for CFL $\simeq 0.6$ and this is used as a guideline in choosing the size of the time step. Typical non-dimensional time step ($\Delta t U_{\infty}/d$) for the simulations presented here varies from 0.001 to 0.004. Furthermore, the solver operates at 960 Mflops on 1 CPU of the CRAY T-90 and requires about 8 μs per grid point per time step. Steady simulations of flow past spheroids have also been performed and comparisons made with available numerical data.

3.1. Simulations of flow past spheres

3.1.1. Spatial accuracy. A series of simulations of flow past a sphere have been carried out in order to demonstrate the high spatial accuracy of the solver. An axisymmetric flow configuration with $Re_d = 100$ has been used to test grid convergence in the wall-normal and -tangential direction. We first simulate this flow on a dense $121 \times 128 \times 2$ ($N_\xi \times N_\eta \times N_\phi$) mesh to obtain a solution with high accuracy and this is used as the reference for computing the errors on coarser meshes. A relatively small Δt of 0.0015 is used and the solution integrated forward in time to $30d/U_\infty$. Furthermore, a uniform mesh is used in the η-direction so as to simplify the convergence analysis. In order to check the accuracy in the wall-normal direction, the number of collocation points in the η-direction is fixed at 128 and the number of collocation points in the wall-normal direction reduced successively. The solution is computed on each of these coarse meshes and the root-mean-square difference between this solution and the reference solution normalized by the number of wall-normal collocation points provides an estimate for the truncation error in the computed solution. For the wall-normal test we compute this error along the wake centreline, and Figure 3 shows the error in the wall-normal component of velocity plotted against the number of collocation points in the wall-normal direction. As expected, exponential convergence is obtained. The convergence test for the η-direction proceeds in a similar way by fixing the number of wall-normal collocation points to 121 and successively coarsening the grid in the tangential direction. An η-grid line is chosen in the near-wake where there are significant tangential gradients and the errors computed on this grid line. Figure 3 shows the errors in the wall-normal component velocity plotted against the number of tangential collocation points and again we observe exponential convergence.

With the pole filtering strategy adopted here we expect some deterioration in the local accuracy of the solver. However, since the filtering comes into effect only in a limited region in the very near-wake, we also expect that the global accuracy will not be affected substantially. In order to test this, we have performed a series of simulations of a non-axisymmetric configuration that consist of a flow past a sphere at an angle-of-attack of 5°. A $61 \times 64 \times 48$ ($N_\xi \times N_\eta \times N_\phi$) mesh is used to compute the reference solution and the pole filtering is turned off in this simulation. Subsequently, the pole filtering is turned on and the solution computed on a series of meshes with fewer azimuthal collocation points. The global error for each mesh is then computed by calculating the root-mean-square difference between the computed solution and the reference solution and this is normalized by the total number of collocation
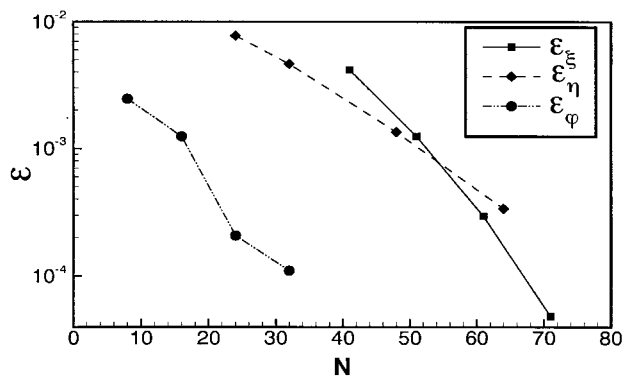

Figure 3. Semi-log plot of error (ε) vs. number of collocation points (N) that shows exponential convergence in all three directions.
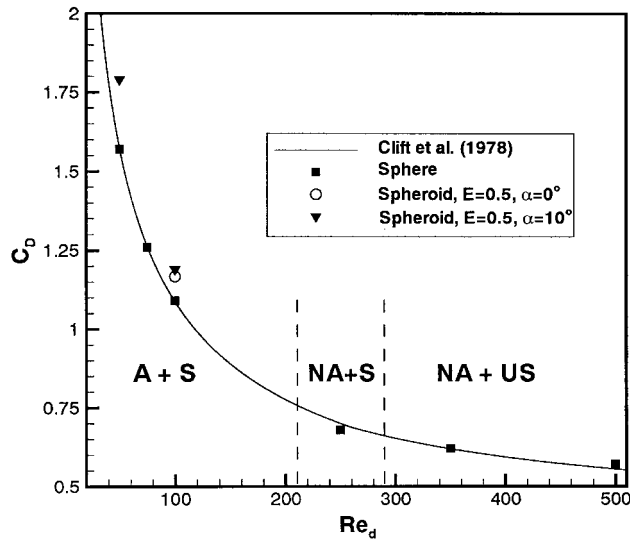
Figure 4. Comparison of computed drag coefficient with the experimental correlation of Clift *et al.* [35]. Computed drag coefficient for spheres as well as spheroids is shown, The various flow regimes for sphere wakes are also indicated on this plot. A, Axisymmetric; NA, non-axisymmetric; S, steady and US, unsteady.

points in the domain. This error is also plotted in Figure 3 and we find that the convergence is not as regular as in the other two directions. However, there is an exponential decrease in the error with increasing collocation points and this confirms that the pole filtering strategy does not have a deleterious effect on the global order of accuracy.

3.1.2. Axisymmetric simulations. Experiments [6,33] and stability analyses [34] shows that the sphere wake in a uniform flow remains axisymmetric up to a Reynolds number of about 210. Three simulations of flow past a sphere have been carried out in this regime and numerical values of the drag coefficient are given in Table I. In addition, the plot in Figure 4 shows the drag coefficient for all the simulations presented in this study. We find that the computed drag coefficient shows excellent agreement with the experimental correlation of Clift *et al.* [35]. Also included in the table are the grids used for the various simulations and the outer radius of the computational domain (R_o) The separation angle measured from the rear stagnation point has also been computed and is found to be within 1° of the corresponding angle given in Clift *et al.* [35] and within 2° of the values obtained in the simulations of Tomboulides *et al.* [2]. Finally, the length of the standing eddy (L_e) measured from the base of the sphere is also compared with the numerical results of Pruppacher *et al.* [36] and very good agreement is observed. The corresponding values obtained by Tomboulides *et al.* [21] have also been shown in the table and it is found that their values are somewhat underpredicted at the lower Reynolds numbers.

3.1.3. Non-axisymmetric simulations. Natarajan and Acrivos [34] investigated the linear stability of the steady axisymmetric flow past a sphere and found that the flow undergoes a regular bifurcation at a Reynolds number of about 210, which results in the development of a non-axisymmetric wake. However, in contrast to the circular cylinder wake, loss of symmetry in the sphere wake does not necessarily lead to vortex shedding. Flow visualization studies [6,37] that use dye injected from the cylinder surface show that this flow regime is characterized by two tails of dye that extend from the end of the recirculation zone in the downstream

Table I. Comparison of computed results of flow past a sphere with experimental and numerical data.

Re_d	$N_\xi \times N_\eta \times N_\phi$	R_o/d	Current simulations			Experiments/other simulations					Flow
			C_D	θ_s (°)	L_e/d	C_D [a]	θ_s [c] (°)	θ_s [c] (°)	L_e/d [b]	L_e/d [c]	
50	$81 \times 60 \times 2$	15	1.57	39.8	0.44	1.57	40.7	40.5	0.45	0.40	A, S
75	$81 \times 60 \times 2$	15	1.26	47.2	0.72	1.26	48.6	49.0	0.72	0.66	A, S
100	$81 \times 60 \times 2$	15	1.09	52.3	0.87	1.09	53.4	54.0	0.90	0.87	A, S
250	$81 \times 60 \times 16$	15	0.68	66.2	1.6	0.70	66.5	—	—	—	NA, S
350	$81 \times 80 \times 32$	15	0.62	70.5	—	0.60	70.6	—	—	—	NA, S
500	$121 \times 80 \times 32$	22.5	0.57	73.4	—	0.55	74.4	—	—	—	NA, US

A, Axisymmetric; NA, non-axisymmetric; S, steady; US, unsteady.
[a] Clift *et al.* [35]; [b] Pruppacher *et al.* [36]; [c] Tomboulides *et al.* [21].

direction and this has been termed as the 'double-thread' wake. Furthermore, experiments [6,33] indicate that the double thread wake is stable up to a Reynolds number of about 280, which corresponds well with the Hopf bifurcation that Natarajan and Acrivos [34] find at a Reynolds number of 277.

Here we have performed one simulation at a Reynolds number of 250 that lies in the middle of the steady non-axisymmetric regime. A symmetric flow is obtained first and subsequently a small perturbation is given in the near wake for a short time period. This disturbance grows under the influence of the instability mechanism until a saturated state is reached. As expected, a non-axisymmetric steady state is attained. The drag and separation angle obtained are compared with experimental results in Table I and good agreement is obtained. In addition, Figure 5 shows a contour plot of u_ϕ for this flow and we find that it qualitatively compares well with the spatial form of the eigenfunction corresponding to the steady non-axisymmetric mode found by Natarajan and Acrivos [34] and shown in Figure 8(a) of their paper.

Two non-axisymmetric simulations have been performed at Reynolds number of 350 and 500. The grid and domain size employed in these simulations are indicated in Table I. At these Reynolds numbers, the sphere wake exhibits strong vortex shedding and this allows us to validate the solver in the unsteady regime. For both these simulations, a mean axisymmetric flow is obtained first and subsequently a small non-axisymmetric disturbances is provided for a short time in the near wake. The disturbance grows in time due to the inherent instability of
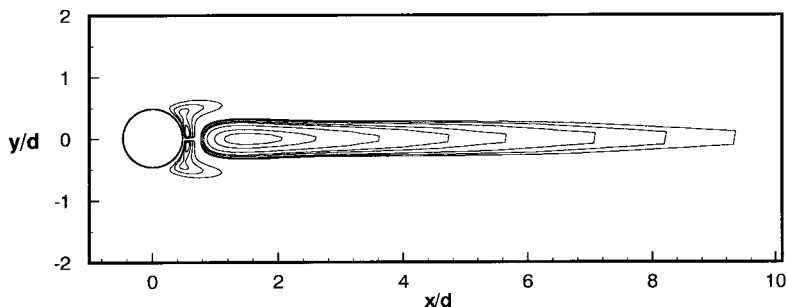

Figure 5. Contour plot of the azimuthal component of velocity u_ϕ, for flow past a sphere at $Re_d = 250$. Natarajan and Acrivos [34] have computed the eigenfunction corresponding to the most unstable mode in this steady, non-axisymmetric regime. The azimuthal velocity corresponding to this mode is shown in Figure 8(a) of their paper and it compares well with the contours obtained in the current simulation.
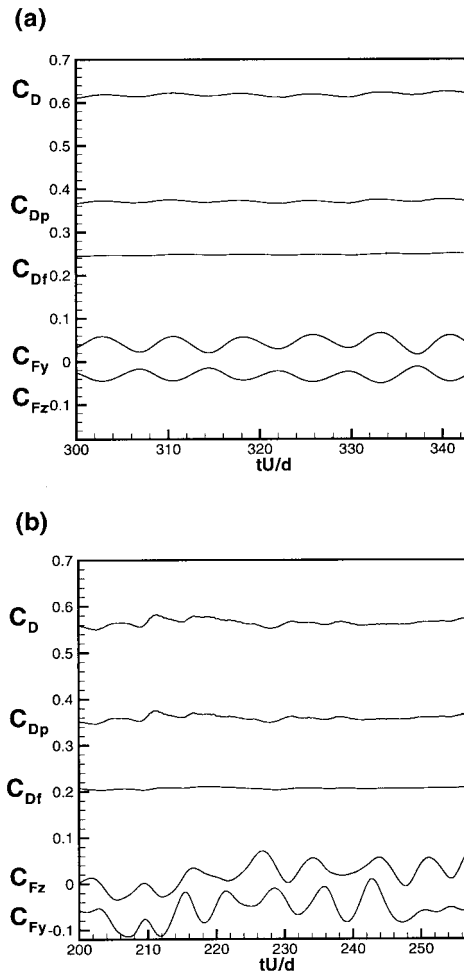
(a)

(b)

Figure 6. Time variation of drag and side-force coefficients computed from simulations of flow past a sphere. (a) $Re_d = 350$ (b) $Re_d = 500$.

the flow and the simulations are continued well beyond the time where a stationary flow is obtained. The mean drag and separation angle obtained from these simulations are tabulated in Table I and we find good agreement with experimental results. The time variation of the force coefficients for both these flows has been shown in Figure 6 and a number of interesting observations can be made. First, we find that in contrast to the cylinder wake where the maximum lift force is comparable with the drag force [38], in the sphere wake, the side force on the sphere is about an order of magnitude smaller than the drag force. This has significance in the context of fluid–structure interactions since it implies that the sideways motion of spheres immersed in a uniform flow would be quite small and could perhaps be neglected in some applications. Secondly, the presence of vortex shedding is most evident through the oscillatory nature of the side force. This plot, therefore, also indicates that vortex shedding is more organized at the lower Reynolds number since the side forces vary in a periodic manner for $Re_d = 350$, whereas the variation of the side force for $Re_d = 500$ indicates a more chaotic shedding process.

In contrast to conventional lower-order methods, spectral methods accurately resolve most of the scales that can be represented on the mesh and this is particularly useful for studying the intricate details of the vortex dynamics of these complex flows. Vortex shedding in the sphere wake is an extremely complicated phenomenon and our knowledge of the mechanism of vortex formation and vortex dynamics in the sphere wake is quite limited. Experiments [6,8] indicate that the unsteady sphere wake undergoes a sequence of distinct transitions in a short Reynolds number range between 300 and 1000 and with each transition, the vortex shedding becomes increasingly complex. Here we examine the vortical structures obtained in the current simulations and compare them with those observed in experiments.

A number of different techniques can be used for identifying and extracting vortical structures. The most straightforward approach is to visualize contours of vorticity. However, with this approach, regions of high strain rate, like, for example, boundary layers, are the main features that are extracted and these might not correspond to regions with high rotation. Furthermore, regions of high strain extracted through this method can hide the real topology of the vortical structures. In the visualization of three-dimensional vortical structures in cylinder wakes [39,40], it has been found that identifying vortical structures by the imaginary part of the eigenvalue of the velocity gradient tensor (denoted by λ_i) brings out the vortex topology in a clear and crisp manner. As shown by Chong $et\ al.$ [4] and Dallmann $et\ al.$ [42] complex eigenvalues of the deformation tensor are found in regions where the rotation dominates over strain and the streamlines are locally circular. Thus, the imaginary part of the complex eigenvalues of the deformation tensor can be used to identify vortical structures. In the figures presented here, vortical structures in the sphere wake have been visualized by plotting one isosurface of λ_i. For further details on this method, the reader is referred to the papers by Chong $et\ al.$ [41] and Dallmann $et\ al.$ [42].
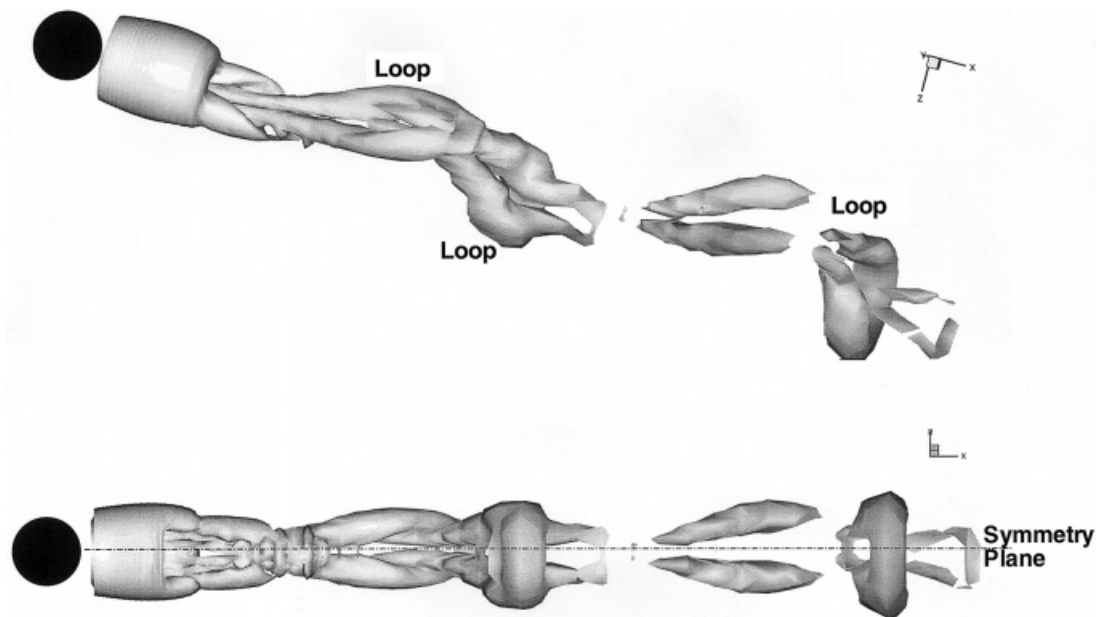

Figure 7. Two views of the vortex topology observed in the wake of a sphere at $Re_d = 350$. The vortical structures have been visualized by plotting one isosurface of λ_i corresponding to a value of 0.1. (a) Perspective view of the wake which shows the interconnected loop structure of the vortices. (b) View along the plane of symmetry. The symmetry plane is indicated by a dash–dot line. The isosurface has been terminated near the sphere surface so as to clearly show the position of the sphere.
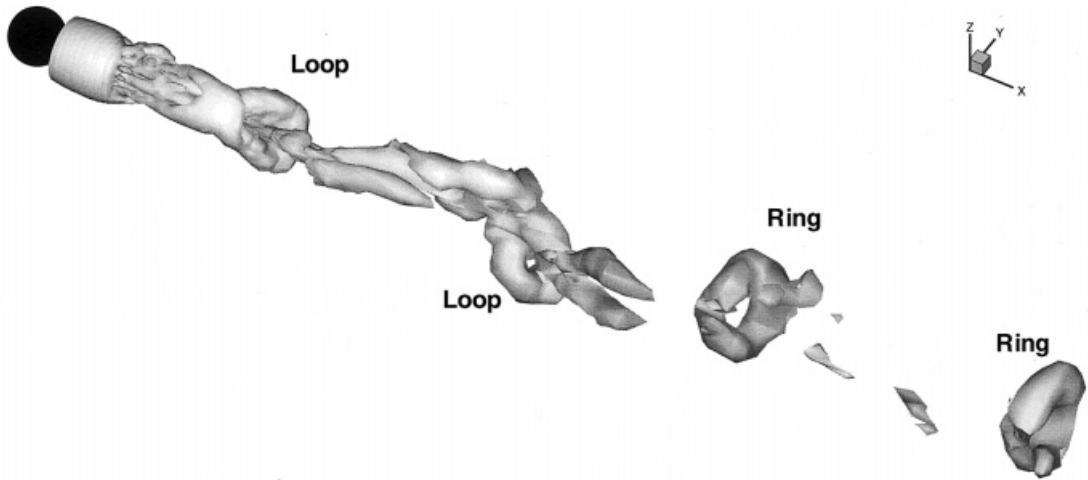
Figure 8. Perspective view of the vortex topology observed in the wake of a sphere at $Re_d = 500$. The vortical structures have been visualized by plotting one isosurface of λ_i corresponding to a value of 0.06. The figure shows the absence of planar symmetry in the near wake and the formation of vortex rings in the downstream region of the wake. The isosurface has been terminated near the sphere surface so as to clearly show the position of the sphere.

Figure 7 shows two views of the vortex topology observed for $Re_d = 350$ at one time instant. The most striking feature observed in the bottom view is the apparent symmetry of the wake about a plane passing through the wake centreline. Planar symmetry in the unsteady sphere wake has been observed in experiments in the range $300 < Re_d < 420$ by Sakamoto and Haniu [8] and has also been confirmed in the simulations of Tomboulides *et al.* [21]. In addition to this, recent flow visualizations of Provansal *et al.* [43] also clearly shows the presence of planar symmetry in this range of Reynolds numbers. Change in the orientation of the plane of symmetry can be detected by computing the phase angle between the two component of side force. For this flow we find that the two components are virtually phase locked with negligible change in the phase angle thereby indicating that the flow in the near wake maintains a fixed plane of symmetry at all times during the shedding process. Furthermore, the top figure shows the three-dimensional structure of the wake and it can be seen that vortex shedding is characterized by the appearance of interconnected vortex loops similar in shape to those observed in the experiments [6,8]. The Strouhal number, which is given by $St = fd/U_\infty$, where f is the shedding frequency, is computed from the time variation of the azimuthal component of velocity in the near-wake and is found to be equal to 0.140. The Strouhal number determined in experiments by Sakamoto and Haniu [8,45] at this Reynolds number lies between 0.13 and 0.15, and therefore the Strouhal number predicted by the current simulation is in good agreement with the experiments.

Although extensive tests of the outflow boundary condition have been carried out previously in cylindrical geometries [28], the adequacy of the domain size for the current simulations still needs to be demonstrated. Therefore, in order to check the influence of the domain size and exit boundary condition on the computed flow field, another simulation has been carried out at a Reynolds number of 350. For this simulation, a domain size with $R_o/d = 22.5$ has been chosen and this is 50% larger than the previous simulation. Furthermore, in order to maintain the same nominal resolution as the previous simulation, a $121 \times 80 \times 32$ grid is employed. The mean drag and separation angle computed from this simulation is found to be within 1% of the values obtained on the smaller domain. The Strouhal number depends directly on the

vortex dynamics in the wake is therefore expected to be more sensitive to the domain size. However, we find that the Strouhal number computed in the big domain is virtually identical to that obtained in the small domain simulation. This clearly shows that the outflow boundary condition performs satisfactorily and that a domain size of $R_o/d = 15$ is adequate for the current simulations.

At the higher Reynolds number of 500, experiments [6,8] indicate that the wake does not exhibit any planar symmetry. The vortex loops are formed in a somewhat irregular fashion and the azimuthal location at which these loops are formed changes slowly from cycle to cycle. A similar scenario emerges from our simulation. Figure 8 shows a flow visualization of this wake and it can be observed that flow is more complex than was observed at the lower Reynolds number. The figure shows that the vortex loops have a structure similar to that observed at the lower Reynolds number; however, the loops themselves do not have any preferred orientation. The phase angle for the side forces has been computed and we find that the phase angle drifts continuously in a quasi-periodic fashion. Another interesting feature is the reorganization of these vortex loops into vortex rings in the downstream region of the wake. The presence of vortex rings at these Reynolds numbers has been reported previously only in the experiments of Margavey and Bishop [6] and the current simulation provides the first numerical confirmation of this phenomenon. The computed Strouhal number is about 0.186, which lies within the range of 0.18–0.19 measured by Sakamoto and Haniu [8,45] and also matches reasonably well with the value of 0.176 predicted by Tomboulides *et al.* [21].
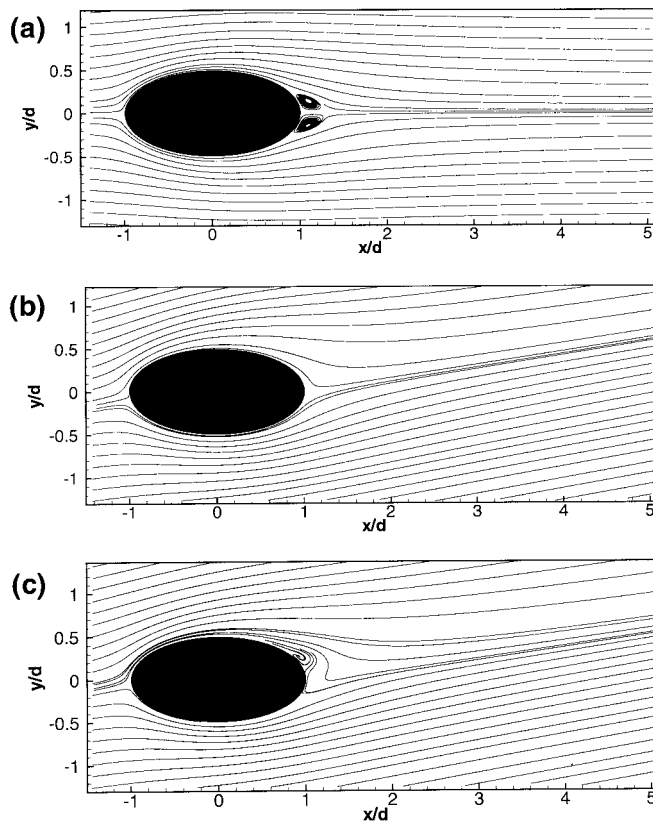

Figure 9. Streamline patterns obtained from simulations of steady flow past a prolate spheroid with aspect ratio $E = 0.5$. (a) $\alpha = 0°$, $Re_d = 100$ (b) $\alpha = 10°$, $Re_d = 50$ (c) $\alpha = 10°$, $Re_d = 100$.

3.2. Simulations of flow past a prolate spheroid

In this study, simulations of flow past spheroids have been limited to the steady regime since the meagre amount of data available on prolate spheroids is limited to numerical results for the zero angle-of-attack, steady flow case. The first simulation carried out is for a prolate spheroid of aspect ratio 0.5 with an angle-of-attack of 0° and Reynolds number of 100. A $81 \times 40 \times 2$ mesh with clustering in the wake is used for this simulation. Figure 9(a) shows the streamline pattern obtained for this flow and it shows the presence of a small symmetric separation bubble. Masliyah and Epstein [45] performed simulations of steady, symmetric flow past prolate spheroids using a second-order finite difference scheme in conjunction with the vorticity–streamfunction formulation. For the same configuration simulated here, they computed an eddy length of 0.31 and a total drag coefficient of 1.18, which compares well with the corresponding prediction from our simulations of 0.29 and 1.17 respectively. Furthermore the ratio of skin friction to form drag found in their simulations was 3.0 and the corresponding value in the current simulation is 2.94. Thus, we find that there is reasonably good agreement between our simulations and the simulation of Masliyah and Epstein [45].

In addition to the zero angle-of-attack simulation, two simulations have been carried out for the same prolate spheroid at an angle-of-attack of 10°. These represent good test cases for evaluating the performance of the solver and the stability of the numerical scheme. In general, grid curvature is more pronounced for ellipsoidal geometries and thus the cross-derivative terms that are treated explicitly are expected to play a more significant role. Furthermore, in flows with non-zero angle-of-attack, there is mean convection across the poles and this is a particularly severe test of the pole filtering strategy. One simulation has been carried out at a Reynolds number of 50 and employs a $81 \times 40 \times 16$. The second simulation is at a Reynolds number of 100 and has been performed on a $81 \times 60 \times 16$ mesh. It is found that both these simulations are stable for CFL $\simeq 0.5$, thereby indicating that the pole filtering strategy is effective even for these simulations. The drag coefficient obtained from these simulations is plotted in Figure 4. It can be seen that at these lower Reynolds number, since the skin friction makes the dominant contribution to the total drag, the drag coefficient for spheroids that have a larger surface area, is higher than the corresponding values for the sphere. The streamline pattern on the symmetry plane for both these simulations is also shown in Figure 9(b) and (c). It is found that there is no flow separation in the symmetry plane at the lower Reynolds number, however, at the higher Reynolds number, a small separation bubble is found. Bifurcation of separation patterns in three-dimensional separated flows is an extremely complicated and interesting subject [1] and an investigation is currently underway to study pattern formation and vortex dynamics in these non-axisymmetric wakes.

4. CONCLUSIONS

A highly accurate Fourier–Chebyshev pseudo-spectral method has been developed for simulating three-dimensional, viscous incompressible flow past spheres and spheroids. The solver employs a Chebyshev scheme in the wall-normal direction and a Fourier scheme in the azimuthal direction. In the other wall-tangential direction, a restricted Fourier series that satisfies the parity conditions across the poles is used. A number of issues including stability condition at the pole, outflow boundary condition and efficient inversion of the pressure Poisson equation have been addressed. In particular, the stability restriction at the poles is relaxed to a large extent by using an approach that combines implicit treatment of selected

terms with low-pass filtering of the velocity field near the poles. The solver has been validated primarily by computing flow past a sphere in the steady as well as unsteady regime and good agreement of critical parameters, like drag coefficient and Strouhal number, is obtained with established experimental [8,35,44] and numerical [21,36] results. Furthermore, it has been shown that the solver is capable of accurately predicting the complex vortex dynamics in the unsteady wake of these three-dimensional bluff-bodies. Simulations of flow past spheroids have been carried out in the stable wake regime and for the zero angle-of-attack, axisymmetric case, we find that our results match reasonable well with the numerical results of Masliyah and Epstein [45].

ACKNOWLEDGMENTS

REFERENCES

1. M. Tobak and D.J. Peake, 'Topology of three-dimensional separated flows', *Annu. Rev. Fluid Mech.*, **14**, 61–85 (1982).
2. F.T. Smith, 'Steady and unsteady boundary layer separation', *Annu. Rev. Fluid Mech.*, **18**, 197–220 (1986).
3. G. Hetsroni, 'Particles–turbulence interaction', *Int. J. Multiphase Flow*, **15**, 735–749 (1989).
4. H.U. Meier, H.P. Kreplin and H. Vollmers, 'Development of boundary layers and separation patterns on a body of revolution at incidence', in T. Cebeci (ed.), *Numerical and Physical Aspects of Aerodynamic Flows*, Session 9, 1983, pp. 1–9.
5. C.E. Costis, N.T. Hoang and D.P. Telionis, 'Laminar separating flow over a prolate spheroid', *J. Aircraft*, **26**, 810–816 (1989).
6. R.H. Margavey and R.L. Bishop, 'Transition ranges for three-dimensional wakes', *Can. J. Phys.*, **39**, 1418–1422 (1961).
7. R.H. Margavey and C.S. MacLatchy, 'Vortices in sphere wakes', *Can. J. Phys.*, **43**, 1649–1656 (1965).
8. H. Sakamoto and H. Haniu, 'A study of vortex shedding from spheres in a uniform flow', *J. Fluids. Eng.*, **112**, 386–392 (1990).
9. T.C. Fu, A. Shekarriz and T.T. Huang, 'The flow structure in the lee of an inclined 6:1 prolate spheroid', *J. Fluid Mech.*, **269**, 79–106 (1994).
10. C.J. Chesnakas and R.L. Simpson, 'Full three-dimensional measurements of the cross-flow separating region of a 6:1 prolate spheroid', *Exp. Fluids*, **17**, 68–74 (1994).
11. K.C. Wang, 'Separation patterns of boundary layer over a inclined body of revolution', *AIAA J.*, **10**, 1044–1050 (1972).
12. K.C. Wang, H.C. Zhou, C.H. Hu and S. Harrington, 'Three-dimensional separated flow structure over prolate spheroids', *Proc. R. Soc. Lond.*, **A421**, 73 (1990).
13. T. Wu and S.-F. Shen, 'Emergence of three-dimensional separation over a suddenly started prolate spheroid at incidence', *AIAA J.*, **30**, 2707–2715 (1992).
14. T. Cebeci and W. Su, 'Separation of three-dimensional laminar boundary layers on a prolate spheroid', *J. Fluid Mech.*, **191**, 47–77 (1988).
15. K. Gee, R.M. Cummings and L.B. Schiff, 'Turbulence model effects on separated flow about a prolate spheroid', *AIAA J.*, **30**, 655–664 (1982).
16. V.C. Patel and J.H. Baek, 'Boundary layers and separation on a spheroid at incidence', *AIAA J.*, **23**, 55–63 (1985).
17. G.A. Glatzmaier, 'Numerical simulations of stellar convective dynamos. I. The model and method', *J. Comp. Phys.*, **55**, 461–484 (1984).
18. D. Bercovici, G. Schubert, G.A. Glatzmaier and A. Zebib, 'Three-dimensional thermal convection in a spherical shell', *J. Fluid Mech.*, **206**, 75–104 (1989).
19. P.N. Swarztrauber, 'On the spectral approximation of discrete scalar and vector functions on the sphere', *SIAM J. Numer. Anal.*, **16**, 934–949 (1979).
20. S.A. Orszag, 'Fourier series on spheres', *Month. Weather Rev.*, **102**, 56–75 (1974).
21. A.G. Tomboulides, S.A. Orszag and G.E. Karniadakis, 'Direct and large-eddy simulations of axisymmetric wakes', *AIAA-93-0546*, 1993.

22. P.E. Merilees, 'A pseudospectral approximation applied to the shallow water equation on a sphere', *Atmosphere*, **11**, 13–20 (1973).
23. S.Y.K. Yee, 'Solution of Poisson's equation on a sphere by truncated double Fourier series', *Month. Weather Rev.*, **109**, 501–505 (1981).
24. C.-M. Tang, 'Comparison of spectral methods for flows on spheres', *J. Comp. Phys.*, **32**, 80–88 (1979).
25. C. Canuto, M.Y. Hussaini, A. Quarteroni and T.A. Zang, *Spectral Methods in Fluid Dynamics*, Springer, Berlin, 1988.
26. A.J. Chorin, 'Numerical solution of the Navier–Stokes equations', *Math. Comput.*, **22**, 745–757 (1968).
27. J. Kim and P. Moin, 'Application of fractional-step method to incompressible Navier–Stokes equations', *J. Comput. Phys.*, **59**, 308–323 (1985).
28. R. Mittal and S. Balachandar, 'Direct numerical simulation of flow past elliptic cylinders', *J. Comput. Phys.*, **124**, 351–367 (1996a).
29. R.L. Sani and P.M. Gresho, 'Resume and remarks on the open boundary condition minisymposium', *Int. J. Numer. Methods Fluids*, **18**, 983–1008 (1994).
30. S.S. Abarbanel, W.S. Don, D. Gottlieb, D.H. Rudy and J.C. Townsend, 'Secondary frequencies in the wake of a circular cylinder with vortex shedding', *J. Fluid Mech.*, **225**, 557–569 (1991).
31. D.B. Haidvogel and T.A. Zang, 'The accurate solution of Poisson's equation by expansion in Chebyshev polynomials', *J. Comput. Phys.*, **30**, 167–180 (1979).
32. J.P. Boyd, *Chebyshev and Fourier Spectral Methods*, Springer, Berlin, 1988.
33. J.-S. Wu and G.M. Faeth, 'Sphere wakes in still surroundings at intermediate Reynolds numbers', *AIAA J.*, **31**, 1448–1455 (1993).
34. R. Natarajan and A. Acrivos, 'The instability of the steady flow past spheres and disks', *J. Fluid Mech.*, **254**, 323–344 (1993).
35. R. Clift, J.R. Grace and M.E. Weber, *Bubbles, Drops and Particles*, Academic Press, New York, 1978.
36. H.R. Pruppacher, B.P.L. Clair and A.E. Hamielec, 'Some relations between drag and flow patterns of viscous flow past a sphere and a cylinder at low and intermediate Reynolds numbers', *J. Fluid Mech.*, **44**, 781–790 (1970).
37. I. Nakamura, 'Steady wake behind a sphere', *Phys. Fluids*, **19**, 5–8 (1976).
38. R. Mittal and S. Balachandar, 'Effect of three-dimensionality on the lift and drag of nominally two-dimensional cylinders', *Phys. Fluids*, **7**, 1841–1865 (1995).
39. R. Mittal and S. Balachandar, 'Generation and evolution of vortical structures in bluff-body wakes', *AIAA 96–0210*, 1996.
40. R. Mittal and S. Balachandar, 'Generation of streamwise vortical structures in bluff-body wakes', *Phys. Rev. Lett.*, **75**, 1300–1303 (1995).
41. M.S. Chong, A.E. Perry and B.J. Cantwell, 'A general classification of three-dimensional flow fields', *Phys. Fluids A*, **5**, 765–777 (1990).
42. U. Dallmann, A. Hilgenstock, S. Riedelbauch, B. Schulte-Werning and H. Vollmers, 'On the footprints of three-dimensional separated vortex flows around blunt bodies', *AGARD CP-494*, 1991.
43. M. Provansal, O. Delphine and B. Analia, 'Spatial structure of the periodic mode in the wake of a sphere', *Bull. Am. Phys. Soc.*, **42**, 2213 (1997).
44. H. Sakamoto and H. Haniu, 'The formation mechanism and shedding frequency of vortices from a sphere in uniform shear flow', *J. Fluid Mech.*, **287**, 151–171 (1995).
45. J.H. Masliyah and N. Epstein, 'Numerical study of steady flow past spheroids', *J. Fluid Mech.*, **44**, 493–512 (1970).